A consistent finite element formulation for laminated composites with nonlinear interlaminar constitutive law

Damjan Lolić [a], Dejan Zupan [b], Miha Brojan [a],*

[a] *University of Ljubljana, Faculty of Mechanical Engineering, Laboratory for Nonlinear Mechanics, Aškerčeva 6, SI-1000 Ljubljana, Slovenia*
[b] *University of Ljubljana, Faculty of Civil and Geodetic Engineering, Jamova 2, SI-1000 Ljubljana, Slovenia*

ARTICLE INFO

ABSTRACT

We introduce a consistent displacement-based finite element formulation for the analysis of laminated composites with nonlinear interlaminar constitutive law. The computational model includes the nonlinear Reissner beam for modelling the bulk material and continuously distributed system of nonlinear springs to describe the connection between layers. We can introduce general functions for describing the stiffness of springs. Therefore, our model is able to describe a variety of physical phenomena, such as friction between layers, contact, cohesive forces, etc. The displacement field on which the stiffness function depends upon is expressed in a local, deformed basis. Distributed force which results from the interaction between layers, is introduced into the governing equations in order to avoid the need for additional interface elements and to simplify the numerical solution method. Precise experiments on thick partially delaminated beam, solid beam, shear lap joint beams and film-substrate composite as well as comparison with the results from the literature, demonstrate the efficiency and versatility of the proposed numerical procedure.

1. Introduction

There is a growing demand for composite materials in many branches of industry, mainly due to their advantageous strength-to-mass ratio and their advantages in the production process. These materials have many applications in mechanical and structural engineering, e.g. for load-bearing elements made of steel-concrete [1], wood-steel [2], fiber-reinforced [3] and woven materials [4] that form entire structures or parts of bridges, roofs, hulls, panels, etc. As their use increases, so does the need to understand their response to mechanical loads and their failure mechanisms, including phenomena such as material interactions, bonding and complex crack propagation. Nevertheless, a review of the literature shows that even symmetric problems, such as the Mode I opening case of a double cantilever beam (DCB), can be challenging for state-of-the-art models, see e.g. [5–7].

The DCB test is an entry-level case for modeling delamination in laminated structures, since its loading induces only normal cohesive forces in the process zone. From an experimental point of view, however, a perfect bond is difficult to achieve due to technological limitations. In order to account for the effects of fabrication imperfections, such as local air entrapment, lack of resin, inclusions, etc., several cohesive zone models (CZM) have been developed since Barenblatt

[8] initially proposed an approach with distributed stress over a finite region near the crack tip and Hillerborg et al. [9] made their finite element implementation. Cubic polynomial [10], trapezoidal [11], smoothed trapezoidal [12], bilinear softening [13], exponential [14] and linear softening [6] cohesive traction-separation models may have equal critical strength and critical energy release rate but each of them will yield a different global response during delamination [15]. However, it is assumed that the influence of CZM parameters is more important than the cohesive model function [16]. With this in mind, Alfano et al. [16] present how different values of cohesive strength and critical energy release rate can be chosen for trapezoidal, bilinear and exponential cohesive models to obtain similar results.

The use of all available mathematical models for cohesive zone modeling requires the prior experimental determination of realistic values of adhesive material parameters. Since the critical energy release rate and the critical cohesive strength are difficult to measure, inverse analyses are very often used to tailor the traction-separation relation to a specific experimental load-displacement curve. Several approaches are used to tackle this problem, e.g. virtual crack-closure method [17], path independent *J*-integral [18], virtual crack extension [19], the stiffness derivative [20] or simply by calibrating the CZM parameters of an idealized cohesive model until a satisfactory

---

agreement between measurements and numerical predictions is obtained, see e.g. works by Liljedahl et al. [21], Alfano et al. [16] and Blackman et al. [22]. Moreover, cohesive model parameters (predicted, derived or measured) are often implemented in finite element code, either by embedding a strong discontinuity in 2D solid elements (see e.g. the work of Manzoli and Shing [23]) or, most commonly, by deriving unconventional finite elements; using CZMs in an interface element formulation. Chen et al. [10], Scheider and Brocks [12], Alfano and Crisfield [6], Camanho et al. [24], Turon et al. [25,26], Lorentz [27], etc. derived additional continuous interface elements with mixed-mode capabilities for the use in conjunction with solid elements. The cohesive elements share common nodes with adjacent upper and lower bodies to carry loads between them. During analysis, the deformation of an element determines its constitutive behavior from initiation of damage to potentially complete failure of the connection. Such formulations usually use two numerical integration procedures: Gaussian quadrature rules for elements representing bulk material and Newton-Cotes integration method for interface elements when a nonlinear traction-separation law is considered. This eliminates unwanted oscillations of the traction field and provides additional manipulation space for fine tuning the simulation and using more integration points in the interface layer.

Following the assumption that the adhesive has lower yielding properties than the base material, one can efficiently model laminated structures with beam theories. The choice of the kinematic model plays an important role in computational efficiency, as discussed by Biel and Stigh [28]. For example, they showed that the calculation of the critical cohesive energy depends more on beam theory than on the parameters of the bilinear cohesive model. They also highlighted the significant differences in the solutions obtained by the Euler-Bernoulli beam model and the 2D plane-stress model. Although the beam model generally cannot capture all the deformation modes that occur in a 2D plane-stress model, Škec et al. [29,30] demonstrate a good agreement between the Timoshenko beam model and the 2D plane-stress model for their set of problems. Williams [31], de Morais [32] and Sun and Pandey [33] use a linear Timoshenko beam on an elastic foundation with linear stiffness characteristics in extension and rotation for use in DCB simulation. Sankar [34] derives a geometrically linear, shear deformable beam element with offset nodes, which is used in the DCB example with discrete nodal connectors for axial and transverse displacements and rotations of the upper and lower beams. Based on the Euler-Bernoulli beam theory, Roche et al. [35] developed a finite element for laminated beams with interlayer slip. Čas et al. [36] and Kryžanowski et al. [37] used shear-stiff Reissner kinematic equations to formulate a two-layer composite beam element and described the interlayer slip in a deformed setting. Their formulation was updated by Kroflič et al. [38] by adding the uplift between the layers to the model. In addition, Schnabl and Planinc [39] also consider both slip and uplift between the two layers of a composite column, but consider a fully nonlinear Reissner beam model.

In the above beam-based models, continuous layers of springs between elements or discrete springs located at the nodes are used to describe the interface between the layers. If the continuous or smeared model is introduced in the main equations, more effort is required to construct the tangent stiffness matrix, as opposed to the discrete spring model, which is treated the same as external forces and added to the construction when the stiffness matrix is already formed. However, to achieve the same effect, the use of discrete model requires more degrees of freedom than the smeared model. As shown by Carpinteri and Massabo [40] and Rots [41] for the case of two-dimensional crack propagation in concrete, both approaches generate the same global results.

In this work, we present a finite element formulation of a composite beam that allows a more accurate modeling of the contact interactions between the layers. The beam formulation is based on the geometrically exact Reissner beam theory, while the interactions

between the layers are described by sufficiently smooth functions along the length of the beam. These interactions vary from rigid to allowable interlayer slip, lift or both. The function of the interaction (stiffness) can be continuous or discontinuous and depends on the relative normal and tangential displacements. The uncoupled displacement field used in the stiffness function is appropriately rotated to account for the large displacements and large rotations. The details are presented in Section 2, where the governing equations, the elastic foundation function and the interface stiffness relations, along with linearization and the construction of the tangent stiffness matrix are derived. Section 3 contains the descriptions of all experiments we have performed. These include: thick cantilever beam experiment, delaminated beams, single lap joint shear test and thin film bonded to a thick compliant substrate. The results found in the available literature, such as for a composite beam with interlayer slip, axially loaded delaminated beam and double cantilever bending test, are compared with our numerical results and discussed in Section 4. Finally, Section 5 summarizes the work done in this study and provides some ideas for future work.

2. Theoretical formulation

We apply the Reissner beam theory [42] to model delamination and complex contact interactions between layers in thick composite beams within finite extensional, bending and shear strains. We limit our analysis to beams made from laminae of isotropic, homogeneous and linearly elastic material and assume that the cross-section of the beam remains planar during loading, while the centroid axis is extensible. We also assume that the beam is initially straight and rotated by angle φ_0 in the global coordinate system, as shown in Fig. 1. Displacement fields in two principal directions are denoted as u and w, while φ represents the rotation of the cross section. The governing equations of this problem are, [42]:

- kinematic equations relating displacements and strains:

$$\cos\varphi_0 + u' = (1+\varepsilon)\cos\varphi - \gamma\sin\varphi, \tag{1}$$
$$\sin\varphi_0 + w' = -(1+\varepsilon)\sin\varphi + \gamma\cos\varphi, \tag{2}$$
$$\varphi' - \varphi_0' = \kappa. \tag{3}$$

- equilibrium equations relating internal and external forces and moments:

$$R_x' + p_x = 0, \tag{4}$$
$$R_y' + p_y = 0, \tag{5}$$
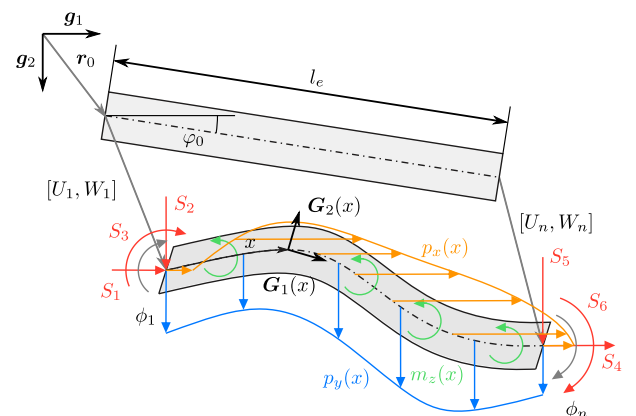$$M' + (1+\varepsilon)Q - \gamma N + m_z = 0, \tag{6}$$

Fig. 1. Initial and deformed shape of a beam element subjected to external nodal and distributed loads.

where R_x and R_y are resultant forces expressed in global basis

$$R_x = N\cos\varphi - Q\sin\varphi, \tag{7}$$
$$R_y = N\sin\varphi + Q\cos\varphi. \tag{8}$$

- constitutive equations for linear elastic material relating stress resultants and strains:

$$N_c = E\int_A (\varepsilon + y\kappa)\,dA, \tag{9}$$

$$Q_c = GA_s\gamma, \tag{10}$$

$$M_c = E\int_A y(\varepsilon + y\kappa)\,dA. \tag{11}$$

Here, symbol $\prime$ represents a derivative with respect to the arc length parameter x. With ε, γ and κ we denote the extensional, shear and bending strain, respectively, p_x, p_y and m_z are the external distributed forces and moment per unit length, N and Q are the internal normal and shear force expressed in a local basis, whereas R_x, R_y and M are the stress resultant forces and moment.

Expression $[\mathbf{S}] = [\mathbf{D}]\,[\boldsymbol{\varepsilon}]$ represents a matrix form of Eqs. (9) and (11), where the strain vector $[\boldsymbol{\varepsilon}] = [\varepsilon, \gamma, \kappa]^T$ and the constitutive forces and moment vector $[\mathbf{S}] = [N_c, Q_c, M_c]^T$ are connected to the constitutive matrix $[\mathbf{D}]$ for linear elastic material as follows:

$$[\mathbf{D}] = \begin{bmatrix} EA & 0 & -ES_y \\ 0 & GA_s & 0 \\ -ES_y & 0 & EI_z \end{bmatrix}. \tag{12}$$

Here, E and G are Young's and shear modulus, respectively. The symbol A_s denotes effective shear area, S_y the first moment of area and I_z the second moment of area. Note that in the case of a composite beam, S_y is not zero for a generic lamina, because the centroid axis does not coincide with the neutral x-axis.

2.1. Finite element method

Unknown displacement functions u, w and cross section rotation φ are interpolated with a linear combination of discrete values U_i, W_i, ϕ_i and shape functions $P_i(x)$, $i \in \{1,\ldots,n\}$. Derivatives with respect to the arc-length parameter x and variations are expressed as follows:

$$u(x) \approx \sum_{i=1}^n P_i(x)U_i, \quad u'(x) \approx \sum_{i=1}^n P_i'(x)U_i, \quad \delta u(x) \approx \sum_{i=1}^n P_i(x)\delta U_i, \tag{13}$$

$$w(x) \approx \sum_{i=1}^n P_i(x)W_i, \quad w'(x) \approx \sum_{i=1}^n P_i'(x)W_i, \quad \delta w(x) \approx \sum_{i=1}^n P_i(x)\delta W_i, \tag{14}$$

$$\varphi(x) \approx \varphi_0 + \sum_{i=1}^n P_i(x)\phi_i, \quad \varphi'(x) \approx \sum_{i=1}^n P_i'(x)\phi_i, \quad \delta\varphi(x) \approx \sum_{i=1}^n P_i(x)\delta\phi_i. \tag{15}$$

The nodal points x_i, $i \in \{1,\ldots,n\}$, are equally spaced along the length of a finite element. Standard Lagrange polynomials are used for shape functions, while integrals are solved numerically using a Newton-Cotes procedure, in which the integration points coincide with nodes of the finite element. The influence of the numerical integration rule is well explained in the work of Alfano and Crisfield [6], and the reason for not using the Gaussian quadrature rules will be evident in later examples.

A finite element can be subjected to external distributed forces p_x, p_y and moment m_z and nodal forces and moments S_i, $i \in \{1,\ldots,6\}$, as shown in Fig. 1.

Finite element equations are derived from the principle of virtual work, [42]:

$$\int_0^{le} (N_c\delta\varepsilon + Q_c\delta\gamma + M_c\delta\kappa)\,dx = \int_0^{le} (p_x\delta u + p_y\delta w + m_z\delta\varphi)\,dx + \sum_{k=1}^6 S_k\delta U_k. \tag{16}$$

Variations of the discretized approximation equations for the displacement and rotation field (13)–(15) are used in the principle of the virtual work (16) and arranged by the primary unknowns:

$$\sum_{i=1}^n \left\{ \int_0^{l_e} (R_x P_i' - p_x P_i)\,dx \right\}\delta U_i +$$
$$+ \sum_{i=1}^n \left\{ \int_0^{l_e} (R_y P_i' - p_y P_i)\,dx \right\}\delta W_i +$$
$$+ \sum_{i=1}^n \left\{ \int_0^{l_e} (M_c P_i' + ((\sin\varphi_0 + w')R_x - (\cos\varphi_0 + u')R_y - m_z)P_i)\,dx \right\}\delta\phi_i =$$
$$= S_1\delta U_1 + S_2\delta W_1 + S_3\delta\phi_1 + S_4\delta U_n + S_5\delta W_n + S_6\delta\phi_n. \tag{17}$$

Following the fundamental theorem of the calculus of variations, we divide Eq. (17) into sub parts presenting equilibrium in appropriate directions. These are later solved in every beam node, indexed with i, $i \in \{1,\ldots,n\}$,

$$^i e = \int_0^{l_e} (R_x P_i' - p_x P_i)\,dx - S_{xi} = 0, \tag{18}$$

$$^{n+i} e = \int_0^{l_e} (R_y P_i' - p_y P_i)\,dx - S_{yi} = 0, \tag{19}$$

$$^{2n+i} e = \int_0^{l_e} (M_c P_i' + [(\sin\varphi_0 + w')R_x - (\cos\varphi_0 + u')R_y - m_z]P_i)\,dx - S_{\varphi i} = 0. \tag{20}$$

With nodal solutions of primary unknowns at hand, one can calculate the beam's deformation state using kinematic Eqs. (1) and (3).

2.2. Beam on elastic foundation

To model the elastic foundation as a distributed (smeared) layer of springs, we add a constraining relation to the main element equations. The elastic foundation is defined in two directions and depends on the related displacement fields, where its stiffness follows the prescribed spring coefficient function in two principal directions $f_x(u)$ and $f_y(w)$. As such

$$^i e = \int_0^{l_e} (R_x P_i' - (p_x - h_x(u))P_i)\,dx - S_{xi} = 0, \tag{21}$$

$$^{n+i} e = \int_0^{l_e} \left(R_y P_i' - \left(p_y - h_y(w) \right)P_i \right)\,dx - S_{yi} = 0, \tag{22}$$

where

$$h_x(u) = \int_0^u f_x(\hat{u})\,d\hat{u}, \tag{23}$$

$$h_y(w) = \int_0^w f_y(\hat{w})\,d\hat{w}, \tag{24}$$

are the foundation stiffness functions in both directions.

Eqs. (20)–(22) are now linearized with respect to the main discrete unknowns of the problem using a directional derivative.

$$^j \delta e = \sum_{i=1}^n \int_0^{l_e} \left(b_1 P_i' P_j' + (f_x(u))P_i P_j \right)\,dx\,\delta U_i +$$
$$+ \sum_{i=1}^n \int_0^{l_e} \left(-b_3 P_i' P_j' \right)\,dx\,\delta W_i +$$
$$+ \sum_{i=1}^n \int_0^{l_e} \left(([b_3(\cos\varphi_0 + u') + b_1(\sin\varphi_0 + w') - R_y]P_i + b_5 P_i')P_j' \right)\,dx\,\delta\phi_i, \tag{25}$$

$$^{n+j} \delta e = \sum_{i=1}^n \int_0^{l_e} \left(-b_3 P_i' P_j' \right)\,dx\,\delta U_i +$$
$$+ \sum_{i=1}^n \int_0^{l_e} \left(b_2 P_i' P_j' + \left(f_y(w) \right)P_i P_j \right)\,dx\,\delta W_i +$$
$$+ \sum_{i=1}^n \int_0^{l_e} \left(([-b_2(\cos\varphi_0 + u') - b_3(\sin\varphi_0 + w') + R_x]P_i + b_4 P_i')P_j' \right)\,dx\,\delta\phi_i, \tag{26}$$

$$
\begin{aligned}
^{2n+j}\delta e =\ & \sum_{i=1}^{n}\int_{0}^{l_{e}}\left(\left(\left[b_{3}(\cos\varphi_{0}+u')+b_{1}(\sin\varphi_{0}+w')-R_{y}\right]P_{j}+b_{5}P_{j}'\right)P_{i}\right)dx\,\delta U_{i}+\\
&+\sum_{i=1}^{n}\int_{0}^{l_{e}}\left(\left(\left[-b_{2}(\cos\varphi_{0}+u')-b_{3}(\sin\varphi_{0}+w')+R_{x}\right]P_{j}+b_{4}P_{j}'\right)P_{i}\right)dx\,\delta W_{i}+\\
&+\sum_{i=1}^{n}\int_{0}^{l_{e}}\left[b_{2}(\cos\varphi_{0}+u')^{2}+b_{1}(\sin\varphi_{0}+w')^{2}+(\cos\varphi_{0}+u')(2b_{3}(\sin\varphi_{0}+w')-R_{y})-\right.\\
&\left.-R_{y}(\sin\varphi_{0}+w')\right]P_{i}P_{j}+(-b_{4}(\cos\varphi_{0}+u')+b_{5}(\sin\varphi_{0}+w'))(P_{i}'P_{j}+P_{i}P_{j}')+b_{6}P_{i}'P_{j}'\right]dx\,\delta\phi_{i}.
\end{aligned}
\tag{27}
$$

Constants b_{k}, $k\in\{1,\ldots,6\}$, contain constitutive tangent matrix components $\mathcal{C}_{11},\mathcal{C}_{12},\mathcal{C}_{21}$ and $\mathcal{C}_{22}$, as derived in e.g. [43]. For linear elastic material, these coefficients are calculated as follows:

$$
\mathcal{C}_{11}=\frac{\partial N_{c}}{\partial\varepsilon}=E\int_{A}\frac{\partial}{\partial\varepsilon}(\varepsilon+z\kappa)dA=EA,
\tag{28}
$$

$$
\mathcal{C}_{12}=\frac{\partial N_{c}}{\partial\kappa}=E\int_{A}\frac{\partial}{\partial\kappa}(\varepsilon+z\kappa)dA=E\int_{A}z\,dA=ES_{y},
\tag{29}
$$

$$
\mathcal{C}_{21}=\frac{\partial M_{c}}{\partial\varepsilon}=E\int_{A}\frac{\partial}{\partial\varepsilon}(z\varepsilon+z^{2}\kappa)dA=E\int_{A}z\,dA=ES_{y}=\mathcal{C}_{12},
\tag{30}
$$

$$
\mathcal{C}_{22}=\frac{\partial M_{c}}{\partial\kappa}=E\int_{A}\frac{\partial}{\partial\kappa}(z\varepsilon+z^{2}\kappa)dA=E\int_{A}z^{2}dA=EI_{y}.
\tag{31}
$$

2.3. Connected elements

We also add penalty stiffness relations in two directions to our formulation. Here, the elements are connected only to neighboring elements. More precisely, pairs of elements A and B are defined at the start of the procedure and remain unchanged throughout the loading process, whereas the intensity of a bond is related to the relative displacement difference

$$
\Delta u_{g}^{A|B}=u_{A}-u_{B},
\tag{32}
$$

$$
\Delta u_{g}^{B|A}=u_{B}-u_{A},
$$

$$
\Delta w_{g}^{A|B}=w_{A}-w_{B},
\tag{33}
$$

$$
\Delta w_{g}^{B|A}=w_{B}-w_{A}.
$$

For the accurate description of large rotations, the reaction forces are rotated with respect to the local/deformed basis G. The global, fixed basis g is defined with two unit-length vectors $g=\{g_{1},g_{2}\}$, while the local basis is represented as $G=\{G_{1}(x),G_{2}(x)\}$. The local basis varies with each material point x, $x\in[0,l_{e}]$, and consequently with respect to the local rotation $\varphi(x)$. The transformation between the two bases is obtained through the use of a 2×2 rotation matrix $R(\varphi)$: for an arbitrary vector a expressed in global basis $a_{G}=R^{T}a_{g}$ or in local basis $a_{g}=Ra_{G}$. We write the stiffness function in vector form $h_{G}(\Delta r_{G})=\int_{0}^{\Delta r_{G}}f_{G}(\Delta\hat{r}_{G})d\Delta\hat{r}_{G}$, where $f_{G}(\Delta r_{G})$ is a function of the smeared spring coefficient with respect to the relative displacement difference vector Δr_{G}, $[\Delta r_{G}]=[\Delta u_{G},\Delta w_{G}]^{T}$ in local basis and

$$
\Delta u_{G}=\Delta u_{g}\cos(\varphi_{P})+\Delta w_{g}\sin(\varphi_{P}),
\tag{34}
$$

$$
\Delta w_{G}=-\Delta u_{g}\sin(\varphi_{P})+\Delta w_{g}\cos(\varphi_{P}).
\tag{35}
$$

To ensure that both elements (A and B) experience the same reaction forces, a mid-plane between the elements is defined as $\varphi_{P}=(\varphi_{A}+\varphi_{B})/2$, depicted with red in Fig. 2. Next, we express the interface functions in the global basis and insert them into the governing equations,

$$
h_{x}(\Delta u_{g})=h_{T}(\Delta u_{G})\cos(\varphi_{P})-h_{N}(\Delta w_{G})\sin(\varphi_{P}),
\tag{36}
$$

$$
h_{y}(\Delta w_{g})=h_{T}(\Delta u_{G})\sin(\varphi_{P})+h_{N}(\Delta w_{G})\cos(\varphi_{P}).
\tag{37}
$$

Here and in the rest of the paper, normal and tangential components will be denoted as subscripts N and T.

Eqs. (21) and (22) now take the form:

$$
{}^{i}e=\int_{0}^{l_{e}}\left(R_{x}P_{i}'-\left(p_{x}-h_{x}(\Delta u_{g})\right)P_{i}\right)dx-S_{xi}=0,
\tag{38}
$$

$$
{}^{n+i}e=\int_{0}^{l_{e}}\left(R_{y}P_{i}'-\left(p_{y}-h_{y}(\Delta w_{g})\right)P_{i}\right)dx-S_{yi}=0
\tag{39}
$$

and linearized Eqs. (32) and (33) are

$$
\delta\Delta u_{g}=\delta u_{A}-\delta u_{B},
\tag{40}
$$

$$
\delta\Delta w_{g}=\delta w_{A}-\delta w_{B}.
\tag{41}
$$

Eqs. (36) and (37) now yield

$$
\begin{aligned}
\delta h_{x}(\Delta u_{g})=\ &\delta h_{T}(\Delta u_{G})\cos\varphi_{P}-\delta h_{N}(\Delta w_{G})\sin\varphi_{P}\\
&-(h_{T}(\Delta u_{G})\sin\varphi_{P}+h_{N}(\Delta w_{G})\cos\varphi_{P})\delta\varphi_{P}=\\
=\ &f_{T}(\Delta u_{G})\cos\varphi_{P}\delta\Delta u_{G}-f_{N}(\Delta w_{G})\sin\varphi_{P}\delta\Delta w_{G}-\\
&-(h_{T}(\Delta u_{G})\sin\varphi_{P}+h_{N}(\Delta w_{G})\cos\varphi_{P})\delta\varphi_{P},
\end{aligned}
\tag{42}
$$

$$
\begin{aligned}
\delta h_{y}(\Delta w_{g})=\ &\delta h_{T}(\Delta u_{G})\sin\varphi_{P}+\delta h_{N}(\Delta w_{G})\cos\varphi_{P}\\
&+(h_{T}(\Delta u_{G})\cos\varphi_{P}-h_{N}(\Delta w_{G})\sin\varphi_{P})\delta\varphi_{P}=\\
=\ &f_{T}(\Delta u_{G})\sin\varphi_{P}\delta\Delta u_{G}+f_{N}(\Delta w_{G})\cos\varphi_{P}\delta\Delta w_{G}+\\
&+(h_{T}(\Delta u_{G})\cos\varphi_{P}-h_{N}(\Delta w_{G})\sin\varphi_{P})\delta\varphi_{P},
\end{aligned}
\tag{43}
$$

where $\delta\Delta u_{G}$ and $\delta\Delta w_{G}$ are obtained from Eqs. (34) and (35), now in the form

$$
\delta\Delta u_{G}=\delta\Delta u_{g}\cos\varphi_{P}+\delta\Delta w_{g}\sin\varphi_{P}+\Delta w_{G}\delta\varphi_{P},
\tag{44}
$$

$$
\delta\Delta w_{G}=-\delta\Delta u_{g}\sin\varphi_{P}+\delta\Delta w_{g}\cos\varphi_{P}-\Delta u_{G}\delta\varphi_{P}.
\tag{45}
$$

The complete variations of the main Eqs. (38) and (39) with respect to the discrete nodal unknowns are obtained by combining Eqs. (40)–(43), (45). We list them in Appendix.

3. Practical experiments

To test our computational method, we performed precision experiments on various elastic structures, including a thick (solid) cantilever beam, a delaminated thick cantilever beam, a single lap joint and a thin film on a soft substrate.

3.1. Thick cantilever beam

A solid beam was fabricated from two component silicone-based elastomer Elite Double 32 from Zhermack. After the liquid mixture
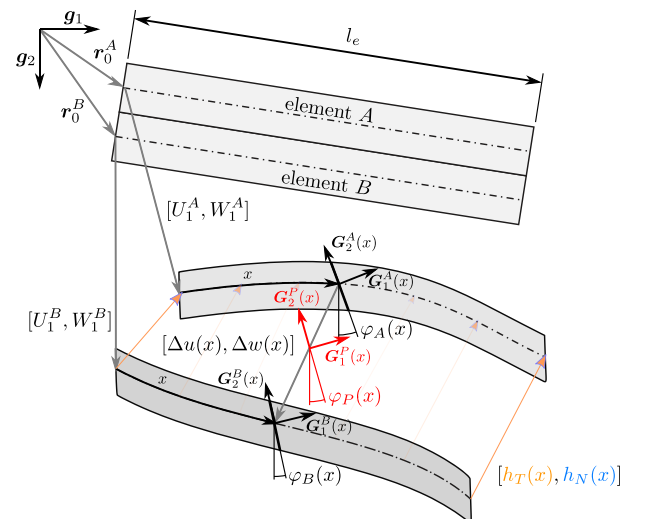

Fig. 2. Undeformed and deformed pair of connected elements A and B.

was poured into the mold (size $320 \times 40 \times 20$ mm), left at the room temperature for approximately half an hour to solidify, it was left in the oven for 12 h at 60 °C to cure. Then a network of lines, representing the beam's centerline and the perpendicular cross-sections was painted on the undeformed beam with a thin white marker. The beam was divided into thirteen 20 mm segments and the intersections between the centerline and cross-sectional lines were marked with small white circles.

Then we performed cantilever bending tests to measure the Young modulus of the beam for 6 different lengths by changing the position of the clamp. The clamp consisted of two solid aluminium blocks that were bolted together and fixed the beam in the middle. To prevent the beam from being compressed by the two blocks, rigid spacers of the same thickness as the beam were placed between them. In Fig. 3a) we show a photo of the cantilever beam with the length $L = 260$ mm. For each of the 6 tests, we took a snapshot of the deformed configuration and traced out the vertical displacement at the free end of the beam with the use of Image Processing Toolbox in Matlab, [44]. The obtained displacement was then used as input data in our numerical model to determine the Young modulus. From the six measurements we obtained $E = 1.369 \pm 0.05$ Mpa. With this value of E we calculated the displacements and rotations for each segment of the beam. Note that here the Young and shear moduli were assumed for homogeneous, isotropic and linear elastic material that is nearly incompressible (as commonly accepted in the literature for this rubber-like material). Therefore we used $\nu \dot{=} 0.5$.

The results, plotted in Fig. 3a) in solid red lines and circles, show a very good agreement between the experiment and the numerical computations. In fact, all 6 considered lengths and results for the end displacements and rotations listed in Table 1 show a very good agreement between experiments and numerics. On average, the relative error of end displacement in the vertical direction is only 0.84%, while the relative error for the horizontal end displacement and end rotation is 1.943% and 1.901%, respectively (see Table 2 for details).

To further demonstrate the efficiency of our computational model, we plot three diagrams that show horizontal and vertical displacements and rotation of all segments as a function of the 13 nodal position on the centerline in Fig. 3b) for both, experiments and computations. White lines from the experiment were traced out via Matlab Image Processing Toolbox. As we can see, a remarkably good agreement is obtained.

3.2. Delaminated cantilever beam

Using the same procedure as in the previous example, we fabricated a beam with a delaminated region as illustrated in Fig. 4a). The same mold as for the thick solid beam and a 1 mm thick acrylic spacer were used to make the delaminated region with rectangular geometry. The geometric details for the beam are given in Table 3 and the material properties are taken from the previous example.

We have divided the beam into 24 segments: 2 and 4 segments for the solid (undelaminated) region (in the left and right), and two times 9 segments for both layers (top and bottom) in the delaminated region. The same structure was maintained in the numerical model, where each segment was discretized by a 5-node finite element. Figure 4b) shows the finite element discretization of the domain. The external nodes shared by the successive elements are colored red, except at the left and right edges of the delamination. At these two points (colored blue), three finite elements share a common external node. The external right node of element 2 and external left nodes of elements 3 and 12 are the same (blue circle on the left) and the external nodes of elements 11 and 20 and external left node of element 21 are the same (blue circle on the right). Here, elements 1, 2 and 21–24 have a zero first moment of area, whereas nodes 3–11 and 12–20 have a non-zero first moment of area. Between these elements we simulate the contact with a bilinear characteristic. A high spring stiffness is
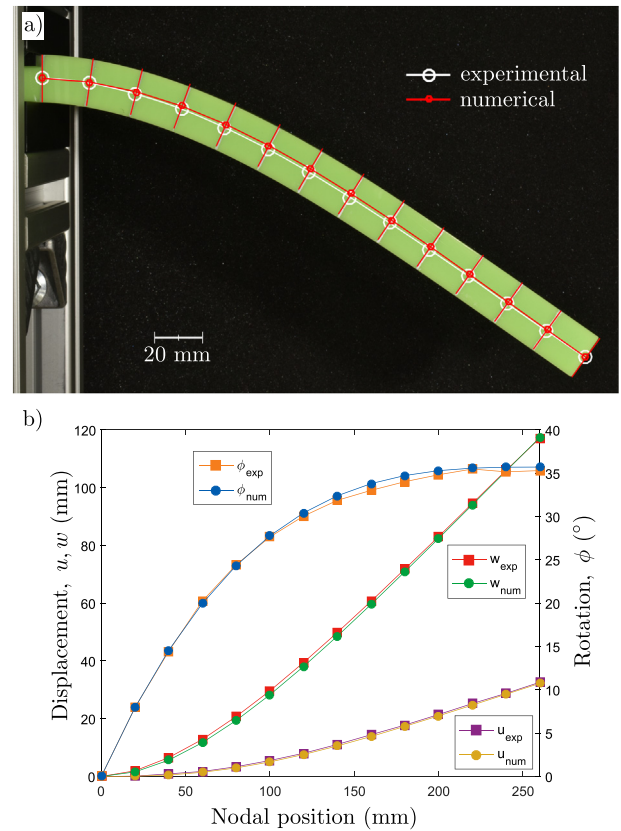

Fig. 3. Experiments on thick cantilever beam subjected to self-weight. a) snapshot of a deformed configuration at length $L = 260$ mm. White lines were painted onto the beam before deformation. Superimposed in red lie the results of the numerical model. b) comparison between experimentally and numerically obtained horizontal displacements u, vertical displacements w and rotations ϕ.

prescribed when the layers are together and zero stiffness when they are separated.

Depending on the up/down orientation, two different experiments were performed on the beam. Figures 5a) and c) show snapshots of the deformed beam configurations with partial delamination between the two layers in two orientations (up and down). In regions where the two layers are in contact, we applied plenty of silicone oil to reduce friction.

In red color we show numerically predicted displacement points and lines that follow the centerlines of both layers, undelaminated regions and the 16 cross-sections. The same points and lines were initially marked with a white marker on the undeformed beam. Again, there is a very good agreement between experiments and computations, as shown in Figs. 5a) and c). To quantify these results, white points and lines were traced out from the photos, as in the previous example and plotted alongside the numerically obtained ones. As can be seen from Fig. 5 good agreement between experimental and numerical results is obtained.

3.3. Single lap joint shear test

The single lap joint shear test is a standard test for adhesives in which the lap shear strength varies along the thickness, toughness and overlap length of the adhesive. To allow a direct comparison between the experimental results and the results of our numerical model, we simplified our experiment by not using a brittle adhesive and by focusing only on the effects of the adhesive thickness and the overlap length on the deformation of the structure.

Table 1
Experimental and numerical results obtained with averaged Young modulus for end displacements and rotations. All results are in milimeters.

	Experimental	Numerical	Experimental	Numerical	Experimental	Numerical
L	160		180		200	
$u(L)$	−1.38	−1.439	−3.27	−3.204	−6.59	−6.460
$w(L)$	19.89	20.211	31.87	31.851	47.39	47.419
$\varphi(L)$	9.15	9.500	13.24	13.398	17.81	18.089
L	220		240		260	
$u(L)$	−12.27	−11.931	−20.29	−20.341	−32.35	−32.228
$w(L)$	68.43	67.111	89.72	90.677	117.03	117.413
$\varphi(L)$	23.36	23.494	28.74	29.448	35.09	35.716

Table 2
Relative error between experimental and numerical results.

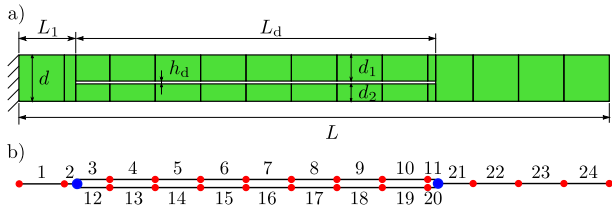|	Relative error (%)		
L (mm)	$u(L)$	$w(L)$	$\varphi(L)$
160	4.275	1.614	3.825
180	2.018	0.060	1.193
200	1.973	0.061	1.567
220	2.763	1.928	0.574
240	0.251	1.067	2.463
260	0.377	0.327	1.784
mean	1.943	0.843	1.901
st. dev.	1.380	0.743	1.033

Fig. 4. Delaminated cantilever beam. a) geometry of the delaminated beam divided into segments. b) discretization of the geometry by 24 5-node finite elements.

We used thin strips (300 × 25 × 0.15) mm made from spring steel with Young modulus $2.1 \cdot 10^5$ MPa and Poisson ratio $\nu = 0.3$ as adherends and an XPS board to fabricate 4 spacers of different thickness and length for bonding with adherends via two-sided adhesive tape. We used XPS material beacuse of its low mass to reduce the loading effect of the spacer.

Both, top and bottom thin strips of spring steel are modeled with ten 4-node finite elements. They are subjected to the distributed load $p_x = 2.89 \times 10^{-4}$ N/mm that represents their mass, while the force of added weights acts at the right end. Elements in the overlapping region (length of the spacer) are connected to the adjacent ones with a stiff connection, thus simulating a rigid XPS spacer. For this example we used constant stiffness law $h_T = h_N = 10$ N/mm.

Figure 6 shows snapshots of 8 deformed single lap joint shear test configurations. Four different adhesive thicknesses are simulated by the XPS spacers. Each spacer configuration is subjected to self-weight and a combination of self-weight and dead load. The numerical results for the left and right thin bars, shown in blue and red, show

excellent agreement with the experiments; practically no mismatch can be observed from the photos.

The effect of adhesive thickness and overlap length is presented in Fig. 7. The diagram shows the angle of overlap rotation as a function of dead weight for each spacer configuration. Four solid curves were obtained numerically and compared with measurements at 6 different dead loads. Each beam was measured 6 times for each of the 6 dead loads. The experimental values were obtained for each experiment from the photos via Matlab Image Processing Toolbox. The mean values (represented by points) and the standard deviation (represented by handles) were calculated. The diagram shows that when the structure is subjected only to self-weight, there is almost no difference between the angle of overlap rotation for 25 × 20 mm and 50 × 20 mm spacer configurations and between the 25 × 10 mm and 50 × 10 mm spacer configurations. The difference between the angle of overlap rotation of both pairs leads to the conclusion that thickness plays a major role when the structure is subjected to small loads, but when the load is greater, the overlap length increasingly affects the results.

Similar conclusions were obtained by da Silva et al. [45,46] in their study of bond strength. They showed that the lap shear strength increases as the bond line becomes thinner. The same as in our case, they found that the use of thinner spacers results in smaller angles and loading of a lap joint mainly by shear stress.

3.4. Wrinkling of a thin film on soft substrate

When a composite of thin elastic film and thick compliant substrate, as illustrated in Fig. 8a), is subjected to a compressive load lower than some critical $p < p_{cr}$, it first compresses and remains flat (Fig. 8b). However, if this structure is further compressed with $p > p_{cr}$ it is more energy efficient for the compressed thin film to bend (wrinkle) into a periodic wave rather that continuing to compress as flat, see Fig. 8c).

We will model this phenomenon with a beam on a continuous foundation of springs, as illustrated in Fig. 8d). A similar approach to solve this stability problem was first applied by Weighardt [47], Biot [48] and Reissner [49].

For an initially flat plate on a soft substrate of infinite thickness, a characteristic wavelength λ of the pattern can be calculated as follows (see e.g. Allen [50]):

$$\lambda = 2\pi h_f \left(\frac{3 - 4\nu_s}{4(1 - \nu_s)^2} \frac{\bar{E}_f}{3\bar{E}_s} \right)^{1/3}, \tag{46}$$

Table 3
Geometrical properties of the delaminated beam. All units are in milimeters.

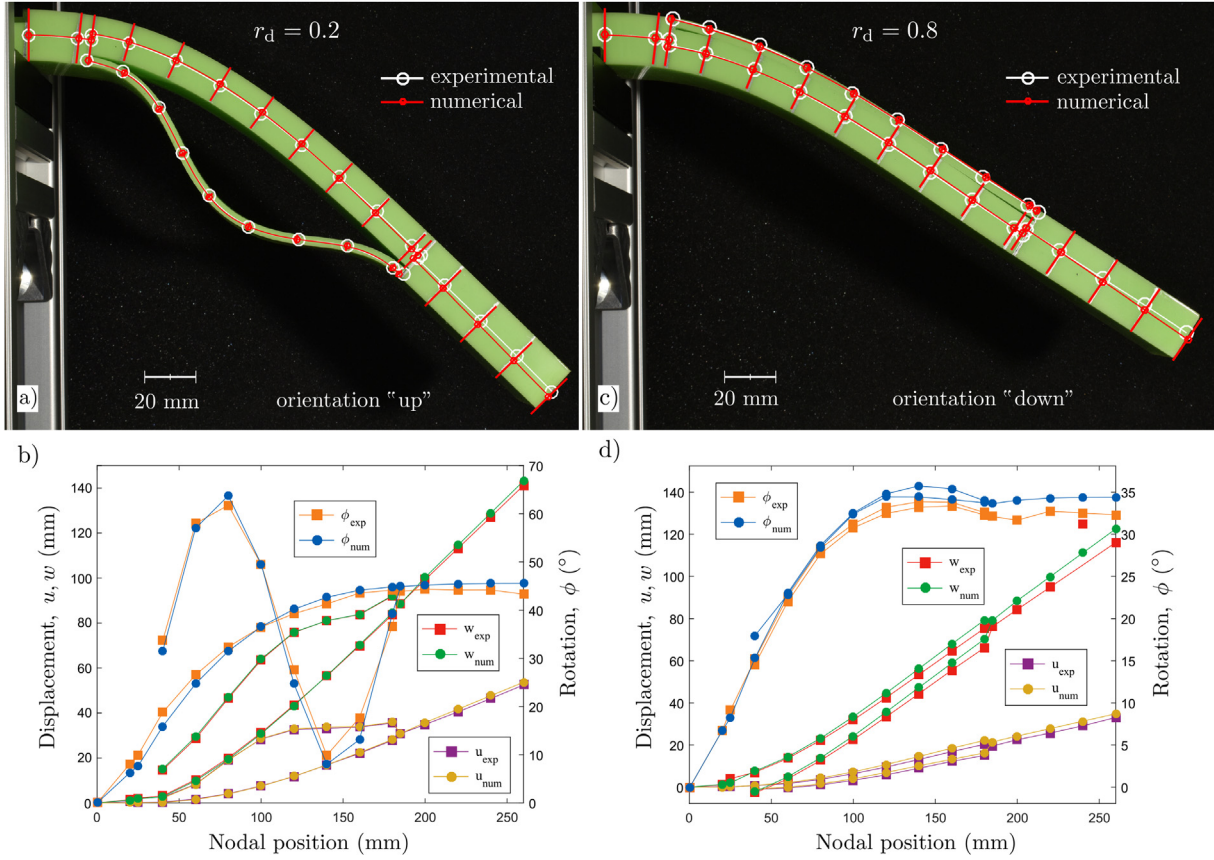| $r_d = d_1/d$	d_1	d_2	h_d	d	b	L_d	L_1	L
0.2	3.68	15.74	1.09	20.51	40.61	158.5	25	260
0.8	15.74	3.68						

Fig. 5. Delaminated thick cantilever beam subjected to self-weight in two orientations. a) snapshot of the deformed beam and b) comparison between experimentally and numerically obtained horizontal displacements u, vertical displacements w and rotations ϕ – both for the beam with thickness ratio $r_d = 0.2$, orientation "up". Analogously, c) and d) represent results for the beam with thickness ratio $r_d = 0.8$, orientation "down".

where

$$\bar{E}_f = \frac{E_f}{1 - \nu_f^2} \quad \text{and} \quad \bar{E}_s = \frac{E_s}{1 - \nu_s^2} \tag{47}$$

are the reduced Young modulus of the film and the substrate, respectively. Here, subscripts f and s denote the film and the substrate, respectively.

For a beam resting on an elastic foundation (see Timoshenko [51]) the characteristic wavelength is:

$$\lambda_{\text{beam}} = 2\pi \left(\frac{k}{E_f I} \right)^{-1/4}. \tag{48}$$

Coefficient of spring stiffness can now be calculated by assuming $\lambda = \lambda_{\text{beam}}$. Equating (46) and (48) thus yields

$$k = \frac{16\pi^4}{\lambda^4} E_f I. \tag{49}$$

According to beam theory [51], the critical buckling force F_{cr} for this problem is:

$$F_{cr} = E_f I \left(\frac{n\pi}{L} \right)^2 + k \left(\frac{L}{n\pi} \right)^2, \tag{50}$$

where

$$n = \frac{L}{\pi} \sqrt[4]{\frac{k}{E_f I}} \tag{51}$$

is a number of (half) waves the deformed beam exhibits after buckling.

For the purpose of our experiment we fabricated the thin film/soft substrate composite from two different polymers, QSil 550 B and Elite

double 8 from Zhermack with the addition of a softener. The structure was fixed between two parallel plates and deformed, as shown in Fig. 9. We used displacement control to induce the deformation.

We measured the material properties of both polymers by tensile and bending tests, and the geometry of the undeformed and deformed beam using digital caliper and Matlab Image Processing Toolbox. Specifically, we measured the Young moduli $E_f = 2.03$ MPa and $E_s = 0.15$ MPa, thickness $h_f = 0.63$ mm and $h_s = 28.94$ mm, width $b = 35.8$ mm, length $L = 100.2$ mm on the undeformed beam and characteristic wavelength of the undulating pattern $\lambda_{\text{exp}} = 6.039$ mm after the composite was compressed by $\Delta L = -10.52$ mm. As before, we considered $\nu \doteq 0.5$ for both materials.

From Eqs. (46)–(51) we can analytically compute the spring stiffness $k = 1.2897$ N/mm^2, the critical force $F_{cr} = 2.7950$ N, the number of waves $n = 30.6$ and the characteristic wavelength $\lambda = 6.541$ mm. Since the formula for λ in Eq. (46) is based on an undeformed length of the beam and the experimental λ_{exp} is measured on a highly deformed beam (of about 10 %), the scaling factor $(L - |\Delta L|)/L = (100.2 - 10.52)/100.2 = 0.895$ should be applied to the analytical solution for a fair comparison. This results in analytically predicted $\lambda_{\text{def}} = 5.854$ mm, which is about 6.6% less than measured in our experiments.

In our numerical model, we used 200 cubic elements to discretize the flat simply supported beam which is connected to a spring foundation with stiffness $k = 1.2897$ N/mm^2 and is subjected to an axial point load at the end of the beam. We employ the arc-length method described by Stanić et al. [52] to solve a system of nonlinear equations. A limit point was detected by observing the sign of the tangent stiffness matrix determinant using a bisection algorithm. A small
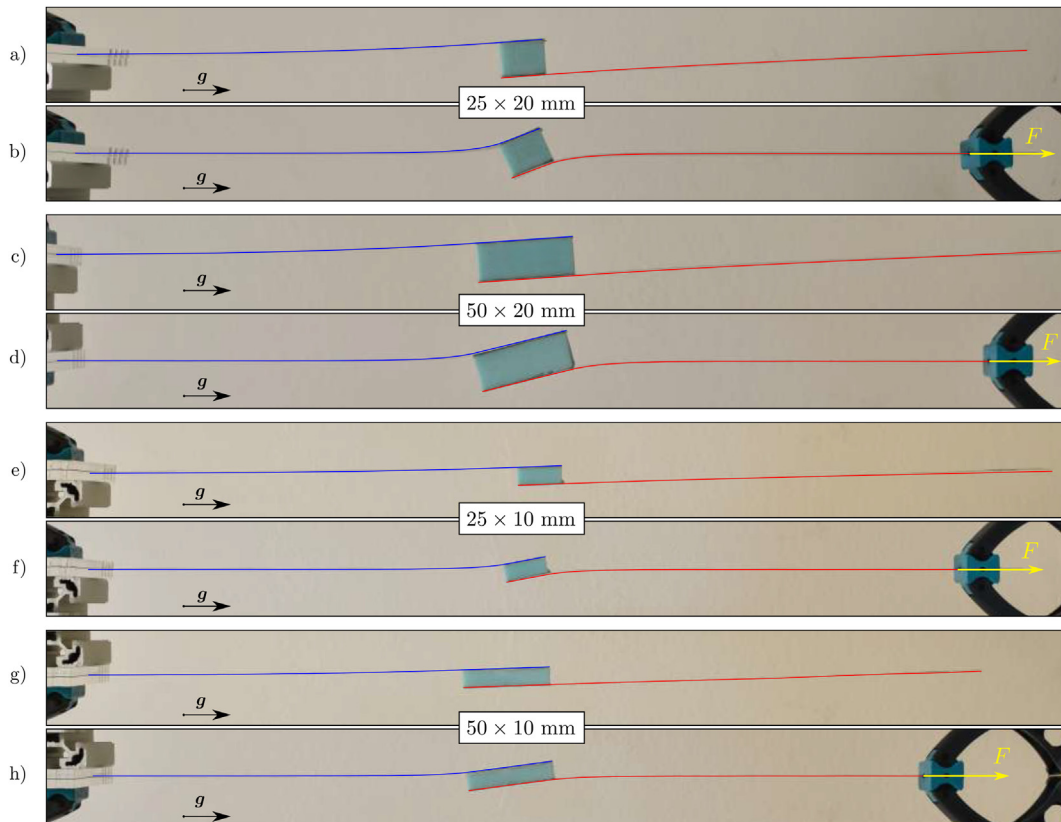
Fig. 6. Thin beams in single lap joint shear test. a) and b) with 25×20 mm spacer, c) and d) with 50×20 mm spacer, e) and f) with 25×10 mm spacer, g) and h) with 50×10 mm spacer. Structures in a), c), e) and g) are subjected to self-weight only, whereas b), d), f) and h) are subjected to a combination of self-weight and dead load. Gravitational force is oriented horizontally as shown with vector **g**.
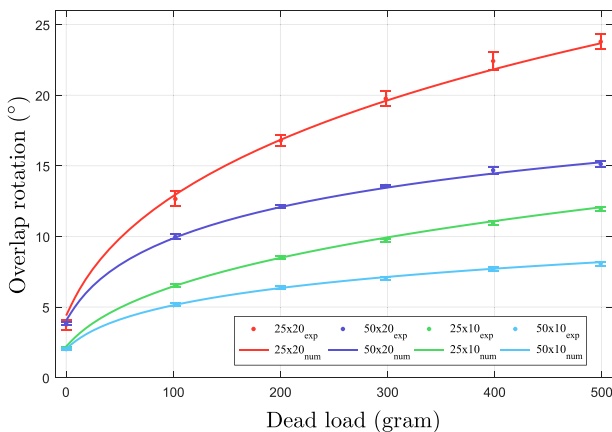

Fig. 7. Comparison of measured and calculated overlap angles for four different spacer dimensions.

perturbation force to incite bending of the beam was added and it was found that the force at the limit point is 2.6181 N, which is approximately 6.3% lower than analytically predicted.

We superimpose the results of our computational model with a solid white line over the photo in Fig. 9. A good agreement between the experiment and the numerical computations can be found along the mid-length of the beam. Note that due to the edge effect, the amplitude near the edge was significantly smaller than in the middle, because the material pressed against the wall cannot deform freely in the vertical direction and as such induces additional stresses and acts as effectively stiffer.
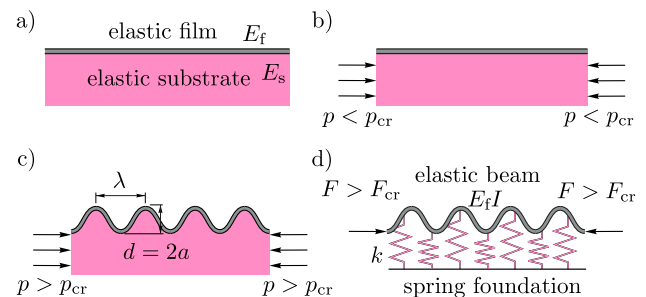

Fig. 8. Wrinkling of a thin film on substrate presented as a beam on elastic foundation of linear springs. a) undeformed configuration. b) subcritical deformation. c) wrinkled structure. d) spring foundation analog.

4. Numerical examples

In this section we attest our numerical model by recomputing the examples from the available literature and compare the results. We focus on different scenarios of two beams interacting through the interface layer. For example, a composite beam with interlayer slip is considered to test the interface modeling with constant stiffness in both directions, an axially loaded delaminated beam to test the ability to model the contact relation as a piece-wise interface function, and as the last example, a double cantilever beam is chosen to test the ability of modeling a bond layer with arbitrary nonlinear model functions.

4.1. Composite with interlayer slip

Figure 10 shows simply supported structure consisting of two beams. They are bonded in such a way that only relative axial displacements are allowed to simulate contact and interlayer slip.
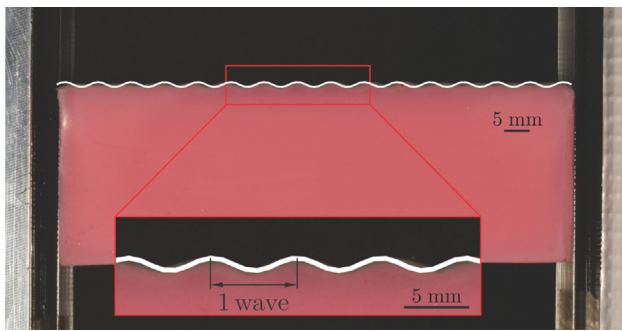
Fig. 9. Photographed wrinkled specimen with end displacement $u(L) = -10.52$ mm. The substrate material is pink and the film (upper thin layer) is gray. Solid white line represents the numerical solution with 200 cubic elements is superimposed onto the photo.

Fig. 10. Axially loaded simply supported composite structure with bottom (1) timber beam and top (2) concrete beam.

Table 4 shows analytical results from Girhammar and Gopu [53], numerical results obtained with two 5-node specially tailored nonlinear finite elements from Čas et al. [36] and numerical results from our computational model, which comprises twenty 5-node elements in each beam. In order to prevent relative normal displacements between the two layers, we used a contact law with constant high penalty stiffness $h_N = 10^9$ N/mm. The stiffness in the axial direction (shear stiffness) is taken from the original paper, using a constant value $f_T = 50$ N/mm^2. Note that the reference results are based on the Euler-Bernoulli beam theory, neglecting shear deformations. Therefore, in our formulation we used an unrealistically large value for the shear modulus $G = 10^9$ MPa for comparison purposes. We also applied shear moduli $G_1 = 3076.9$ MPa for wood and $G_2 = 5000$ MPa for concrete beam to allow for a more realistic response by allowing shear deformations in the beam.

Table 4 shows the results with shear stiffened beams from [53,36] and our computational model with large and realistic shear modulus. We obtained a very good agreement between the results from the literature and our method. We can also observe that the influence of the shear deformation in this problem is small but not negligible.

4.2. Axially loaded delaminated beam

Sheinmann and Soffer [54] studied the effect of geometric imperfection on the post-critical behavior of delaminated beams subjected to axial load. Figure 11 illustrates such a beam in the undeformed configuration. The material is homogeneous, isotropic and linear elastic with $E = 2.1 \cdot 10^5$ MPa and $\nu = 0.3$. The relative length of the delamination is defined by the ratio $l_d = L_d/L = 0.375$ and is positioned in the middle of the beam, lengthwise.

The material points A and B are positioned at the center of the individual layer. In the numerical model, we used 22 cubic elements, i.e. 5 elements for both ends and 6 for each layer. We defined, six pairs of connected elements. At first, we set the stiffness function in the normal direction to zero $f_N = 0$ N/mm^2 so that the layers can move freely. The initial curvature of the beam's centroid axis follows a simple relation

$$v_y(x) = a_i h \sin\left(\frac{\pi x}{L}\right),$$

where h is the height of the cross-section and a_i is the parameter of the imperfection amplitude. Three cases are considered for the parameter of the imperfection amplitude: $a_1 = 0.0001$, $a_2 = -0.00125$ and $a_3 = -0.0625$.

In Fig. 12 we show the load-displacement curves obtained with our computational model for the two characteristic points A and B. The red and blue solid lines represent the results for a_1 and the dashed red and blue lines represent the results for the a_2 imperfection parameter. All four curves are compared with reference data from Ref. [54], which
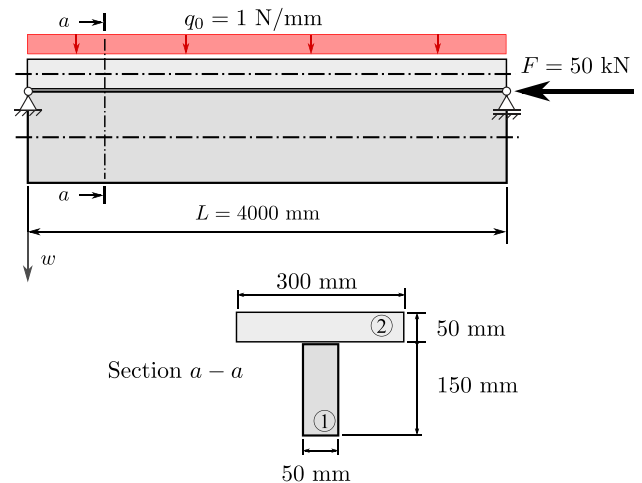
are shown with black lines. A very good agreement is found between all results.

The case with the imperfection parameter a_3 is shown in Fig. 13 in two diagrams. In Fig. 13a) we show the load-displacement curves obtained with our computational model in red and blue color for top and bottom lamina, respectively. Black solid lines represent corresponding results from Ref. [54]. Note that using the model from [54] leads to the cross-penetration of the laminae approximately at $w/L \approx -0.0025$. This non-physical behavior can easily be avoided in our computational model by employing a step function to simulate the contact between laminae. We used an interface bond with zero stiffness when the layers are apart and large numerical value when they coincide. The results of this simulation, illustrated in Fig. 13b), show that the red and blue solid line no longer cross-penetrate. For comparison, we add the results from [54].

4.3. Double cantilever bending test

In this section, we compare the results of our finite element formulation with the numerical results of Alfano and Crisfield [6] for damage of the interface in Mode I delamination. Damage of the interface, associated with the softening part of the cohesive function is identified from load-displacement curves through sharp snap-throughs and snap-backs. These instabilities can cause convergence problems for conventional line search methods. To increase the robustness of a conventional cylindrical arc-length algorithm, Crisfield and co-workers [5,7] proposed alternative criteria for choosing the correct root, the constraint equation or the calculation of the optimal step length. Since the focus of this study is not on the line search method, we used small values for the arc length parameter in the algorithm from Ref. [52] and a small number of allowable iterations in each loading step.

The illustration of the double cantilever bending test is shown in Fig. 14. Geometric and material parameters are given in Table 5. When subjected to a vertical force *F*, the beam of length *L*, with an initial notch length a_0, starts to delaminate as the notch length increases due to failure in the adhesive.

In this test, we apply an exponential and bilinear traction-separation relationship, as shown in Fig. 15 in blue and red solid line, respectively. The stress defined in these formulations is multiplied by the width of an interface on the account that we are dealing with distributed forces: $\sigma_{max} b = F_{max}/l_e$. We assume isotropic linear elastic material instead of orthotropic composite material, as in the referred paper [6].

Table 4
Comparison of analytical and numerical results of a simply supported axially loaded composite beam with interlayer slip.

| | Analytical [53] | FEM E_{5-5} [36] | Present FEM model | |
			$G = 10^9$ MPa	G_1, G_2
w_{max} [mm]	9.276	9.274	9.274	9.312
N_1 [kN]	3.897	3.918	3.920	3.932
N_2 [kN]	-53.897	-53.933	-53.920	-53.932
M_1 [kNm]*	0.6162	0.6157	0.6158	0.7394
M_2 [kNm]*	0.2054	0.2052	0.2052	0.2063
f_{slip} [kN/cm]	13.878	13.881	13.839	13.853

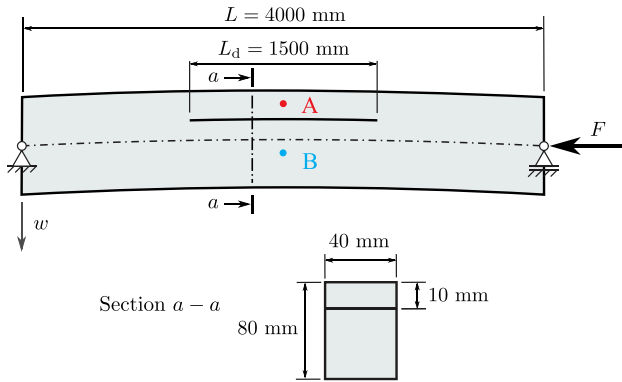* Bending moment with respect to the centroid axis of each layer

Fig. 11. Initially curved delaminated simply supported beam subjected to axial load.
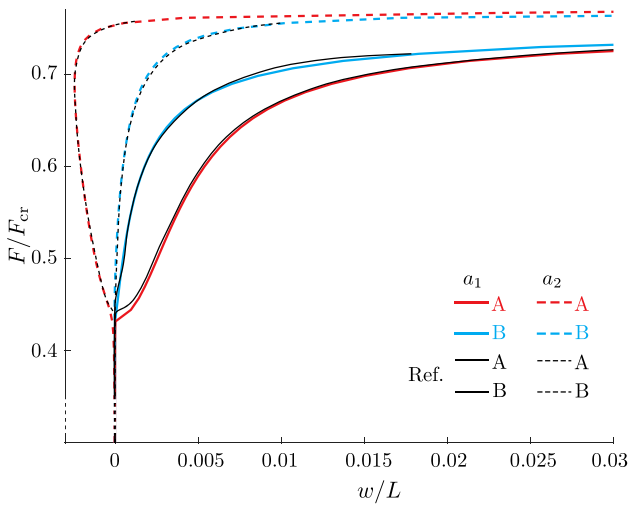

Fig. 12. Load-displacement curves of characteristic points A (upper lamina) and B (lower lamina) for $a_1 = 0.0001$ and $a_2 = -0.00125$. Loads are normalized by Euler buckling load F_{cr} for solid, straight, simply supported beam, displacements are normalized by initial length. The Ref. denotes reference [54].

Fig. 13. Load-displacement curves of characteristic points A (upper lamina) and B (lower lamina) for $a_3 = -0.0625$. a) unrealistic behavior as laminae cross trough each other. b) modeling of a contact. Loads are normalized by Euler buckling load for solid, straight and simply supported beam F_{cr}, displacements are normalized by initial length.

4.3.1. Exponential model

Derived from the potential energy in the crack zone, Xu and Needleman [14] write stiffness function T for a coupled system in two principal directions; normal and tangential. Since we are modeling a symmetrical test where there is no relative tangential displacement and the equation simplifies to

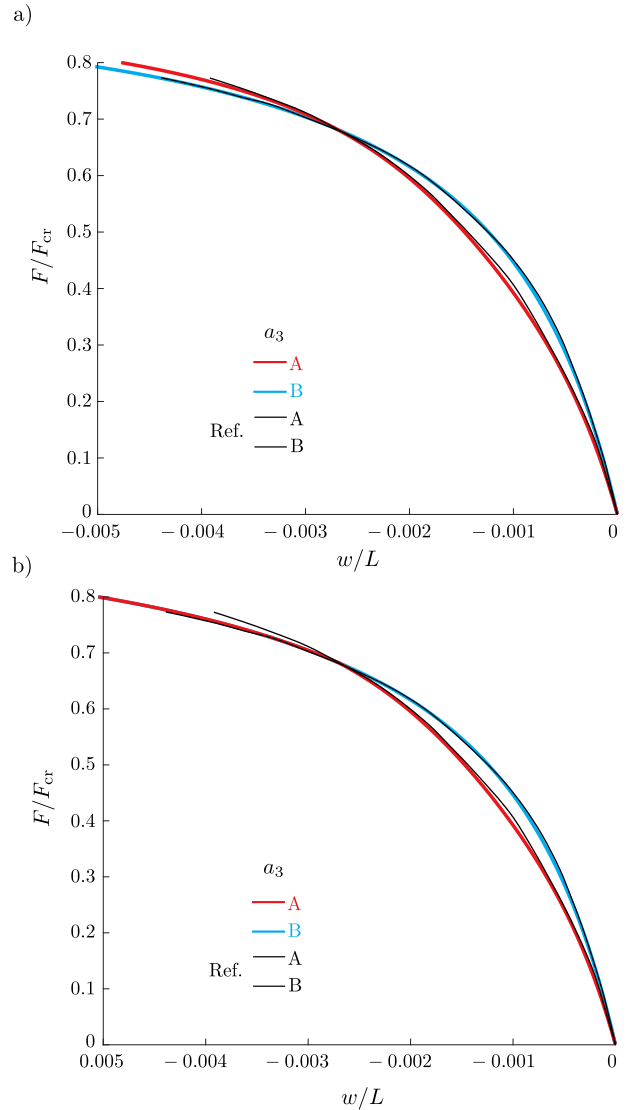$$T_n(\Delta w) = \sigma_{max} \frac{\Delta w}{w_s} \exp\left(1 - \frac{\Delta w}{w_s}\right). \tag{52}$$

Here, σ_{max} represents the maximum cohesive surface normal strength and w_s the corresponding characteristic opening length. Integration of the above equation yields the expression for the normal strain energy release rate:

$$G_I = \int_0^\infty T_n(\Delta w) d\Delta w = \sigma_{max} w_s \exp(1). \tag{53}$$

4.3.2. Bilinear model

The bilinear model with linear hardening and softening parts is the most frequently used in commercial software. It was originally proposed by Hillerborg et al. [9], and Alfano and Crisfield [6]. It is usually expressed as a piece-wise function. To avoid derivative discontinuity, we use the hyperbolic tangent function as a step function to make the transition between softening and hardening part smooth. Therefore

$$T_\mathrm{n}(\Delta w) = \left(0.5 - 0.5\tanh\left(\frac{\Delta w - w_\mathrm{f}}{k_\mathrm{ob}}\right)\right)\left(\frac{\Delta w\sigma_\mathrm{max}\left(0.5 - 0.5\tanh\left(\frac{\Delta w - w_\mathrm{s}}{k_\mathrm{ob}}\right)\right)}{w_\mathrm{s}} + \right.$$
$$\left. + \frac{\sigma_\mathrm{max}(\Delta w - w_\mathrm{f})\left(0.5\tanh\left(\frac{\Delta w - w_\mathrm{s}}{k_\mathrm{ob}}\right) + 0.5\right)}{w_\mathrm{s} - w_\mathrm{f}}\right), \tag{54}$$

where w_f represents the characteristic length of the bond termination and k_ob is a scaling factor for the smoothness of a transition between hardening and softening. The strain energy release rate is thus:

$$G_\mathrm{I} = \frac{\sigma_\mathrm{max}w_\mathrm{f}}{2}. \tag{55}$$

Using Eq. (53) for the exponential model and cohesive zone data from Table 5, we calculated the appropriate opening length $w_\mathrm{s} = 0.0018$ mm. The same value was used in the bilinear model. From Eq. (55) we calculated the characteristic length $w_\mathrm{f} = 0.0098$ mm. Note that the value for w_s used here is much higher than the one from Ref. [6] (where $w_\mathrm{s} = 10^{-7}$ mm was used), but the strain energy G_I, the normal strength σ_max and the length w_f are the same.

A comparison between the results from Ref. [6] (represented in black line) and our formulation (represented with red line for the bilinear law and with blue line for the exponential cohesive law) is displayed in Fig. 16. An inset shows a zoomed-in region from which a very good agreement between the predictions of our computational model and the reference data can be seen for both cohesive models, despite the differences in the material model, the type of elements and the cohesive model parameters. A "zigzag" response obtained in the case of the bilinear law is similar to e.g. [29]. It is interesting to note that the response resulting from the exponential interface law with the same critical energy release rate leads to a significantly smoother curve.

In our simulations we used 120 five-node elements of equal length for each beam with a total of 2886 degrees of freedom. Those located along the initial notch are not connected, while the other 84 pairs
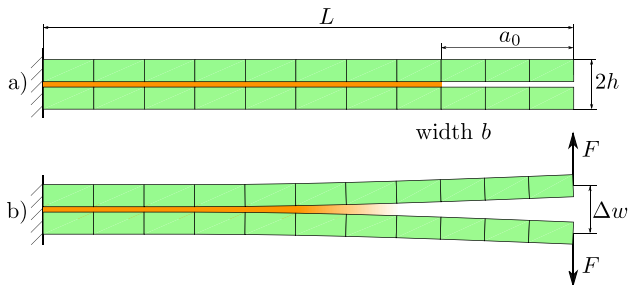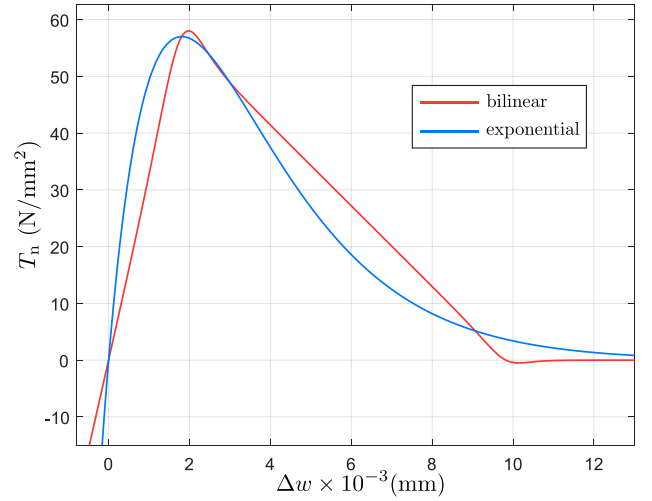

Fig. 15. Bilinear and exponential cohesive model functions with equal critical cohesive energy. Smoothness parameter used in the bilinear model is $k_\mathrm{ob} = 0.0005$.
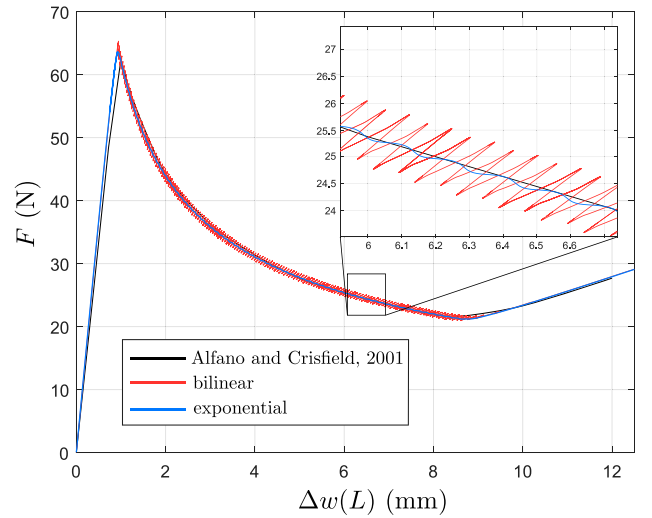

Fig. 16. Force displacement curves for bilinear and exponential interface law and a zoom-in inset.

interact through the adhesion relationship $h_N(\Delta w) = T_\mathrm{n}(\Delta w)$, following either the exponential (see Eq. (52)) or the bilinear law (see Eq. (54)). In comparison, the result from [6] is computed using 4×200 quadrilateral eight-node plane-strain (Q8) elements for the bulk material and 140 six-node interface elements (INT6), which together represent 6420 degrees of freedom. For example, 2406 degrees of freedom were needed in the study by Škec et al. [29], who used interface elements for the adhesive and linear beam elements to model the bulk material to compute approximately the same curve.

From these results we can conclude that the beam elements presented here lead to results comparable to those of 2D plane-stress elements. The deviation in the initial part of the diagram shown in Fig. 16

Fig. 14. A double cantilever beam. a) initial notch length a_0 increases when b) force is applied and adhesive (orange region) starts to fail.

Table 5
Geometrical, material and cohesive zone properties for a DCB test.

L (mm)	a_0 (mm)	b (mm)	h (mm)	E (GPa)	ν	σ_max (MPa)	U_I (N/mm)
100	30	20	1.5	135.3	0.24	57	0.28

is due to the use of an isotropic material model instead of an orthotropic one. The fact that we used a larger value for w_s and a continuous function to describe the bilinear cohesive model has not affected the results. With this in mind, we again emphasize the larger importance and influence of the critical strain energy and cohesive strength than that of the model function parameters.

5. Conclusions

We derived a finite element, based on a nonlinear Reissner beam theory to analyze delaminated beams. The formulation is designed to be consistent, robust and flexible. The connection between the layers is prescribed with an arbitrary function for the stiffness of springs, which are continuously distributed over the length of an element. The displacement field on which the stiffness function depends is expressed in a local deformed basis. Large displacements and rotations are taken into account. The distributed force resulting from the interaction between the layers is included in the governing equations to avoid the need for additional interface finite elements and to integrate the equations with a single numerical method.

The versatility of our computational model and the formulation of the interface layer is demonstrated by a number of numerical and experimental examples. We modeled delamination, contact, friction and cohesion and obtained an excellent agreement between numerical and experimental results. In addition, our computational method justifies the use of beam finite elements, as they use fewer degrees of freedom compared to the most commonly used 2D plane-stress elements and provide comparable results for these types of problems.

CRediT authorship contribution statement

Damjan Lolić: Software, Validation, Investigation, Writing - original draft, Writing - review & editing, Visualization. **Dejan Zupan:** Conceptualization, Writing - review & editing, Supervision. **Miha Brojan:** Conceptualization, Methodology, Validation, Writing - review & editing, Supervision.

Declaration of Competing Interest

The authors declare that they have no known competing financial interests or personal relationships that could have appeared to influence the work reported in this paper.

Acknowledgment

Appendix A

The complete variations of the main Eqs. (38) and (39) with respect to the discrete nodal unknowns.

$$
\begin{aligned}
{}^{j}\delta e = \ & \sum \int_0^{l_e} \left(b_1 P_i^{A\prime} P_j^{A\prime} + (f_T(\Delta u_G)\cos^2(\varphi_P) + f_N(\Delta w_G)\sin^2(\varphi_P)) P_i^A P_j^A \right) dx \delta U_i^A + \\
& + \sum \int_0^{l_e} \left(-b_3 P_i^{A\prime} P_j^{A\prime} + (f_T(\Delta u_G)\sin(\varphi_P)\cos(\varphi_P) - f_N(\Delta w_G)\sin(\varphi_P)\cos(\varphi_P)) P_i^A P_j^A \right) dx \delta W_i^A + \\
& + \sum \int_0^{l_e} \Big(((b_3(\cos(\varphi_0)+u') + b_1(\sin(\varphi_0)+w') - R_y) P_i^A + b_5 P_i^{A\prime}) P_j^{A\prime} + \\
& \quad + \tfrac{1}{2}(f_T(\Delta u_G)\Delta w_G \cos(\varphi_P) + f_N(\Delta w_G)\Delta u_G \sin(\varphi_P) - h_y(\Delta w_g)) P_i^A P_j^A \Big) dx \delta \phi_i^A + \\
& + \sum \int_0^{l_e} \left(-f_T(\Delta u_G)\cos^2(\varphi_P) - f_N(\Delta w_G)\sin^2(\varphi_P) \right) P_i^B P_j^A dx \delta U_i^B + \\
& + \sum \int_0^{l_e} \left(-f_T(\Delta u_G)\cos(\varphi_P)\sin(\varphi_P) + f_N(\Delta w_G)\sin(\varphi_P)\cos(\varphi_P) \right) P_i^B P_j^A dx \delta W_i^B \\
& + \sum \int_0^{l_e} \tfrac{1}{2}(f_T(\Delta u_G)\Delta w_G \cos(\varphi_P) + f_N(\Delta w_G)\Delta u_G \cos(\varphi_P) - h_y(\Delta w_g)) P_i^B P_j^A dx \delta \phi_i^B,
\end{aligned}
\tag{56}
$$

$$
\begin{aligned}
{}^{n+j}\delta e = \ & \sum \int_0^{l_e} \left(-b_3 P_i^{A\prime} P_j^{A\prime} + (f_T(\Delta u_G)\sin(\varphi_P)\cos(\varphi_P) - f_N(\Delta w_G)\cos(\varphi_P)\sin(\varphi_P)) P_i^A P_j^A \right) dx \delta U_i^A + \\
& + \sum \int_0^{l_e} \left(b_2 P_i^{A\prime} P_j^{A\prime} + (f_T(\Delta u_G)\sin^2(\varphi_P) + f_N(\Delta w_G)\cos^2(\varphi_P)) P_i^A P_j^A \right) dx \delta W_i^A + \\
& + \sum \int_0^{l_e} \Big(((-b_2(\cos(\varphi_0)+u') - b_3(\sin(\varphi_0)+w') + R_x) P_i^A + b_4 P_i^{A\prime}) P_j^{A\prime} + \\
& \quad + \tfrac{1}{2}(f_T(\Delta u_G)\Delta w_G \sin(\varphi_P) - f_N(\Delta w_G)\Delta u_G \cos(\varphi_P) + h_x(\Delta u_g)) P_i^A P_j^A \Big) dx \delta \phi_i^A + \\
& + \sum \int_0^{l_e} \left(-f_T(\Delta u_G)\sin(\varphi_P)\cos(\varphi_P) + f_N(\Delta w_G)\sin(\varphi_P)\cos(\varphi_P) \right) P_i^B P_j^A dx \delta U_i^B + \\
& + \sum \int_0^{l_e} \left(-f_T(\Delta u_G)\sin^2(\varphi_P) - f_N(\Delta w_G)\cos^2(\varphi_P) \right) P_i^B P_j^A dx \delta W_i^B \\
& + \sum \int_0^{l_e} \tfrac{1}{2}(f_T \Delta(u_G)\Delta w_G \sin(\varphi_P) - f_N(\Delta w_G)\Delta u_G \cos(\varphi_P) + h_x(\Delta u_g)) P_i^B P_j^A dx \delta \phi_i^B.
\end{aligned}
\tag{57}
$$

References

[1] Spacone E, El-Tawil S. Nonlinear analysis of steel-concrete composite structures: State of the art. J Struct Eng 2004;130(2):159–68.

[2] Yeoh D, Fragiacomo M, De Franceschi M, Heng Boon K. State of the art on timber-concrete composite structures: literature review. J Struct Eng 2011;137(10):1085–95.

[3] Sen R, Liby L, Mullins G. Strengthening steel bridge sections using CFRP laminates. Compos Part B-Eng 2001;32(4):309–22.

[4] Mountasir A, Hoffmann G, Cherif C, Löser M, Großmann K. Competitive manufacturing of 3D thermoplastic composite panels based on multi-layered woven structures for lightweight engineering. Compos Struct 2015;133:415–24.

[5] Hellweg HB, Crisfield MA. A new arc-length method for handling sharp snap-backs. Comput Struct 1998;66(5):704–9.

[6] Alfano G, Crisfield MA. Finite element interface models for the delamination analysis of laminated composites: mechanical and computational issues. Int J Numer Meth Eng 2001;50(7):1701–36.

[7] Alfano G, Crisfield MA. Solution strategies for the delamination analysis based on a combination of local-control arc-length and line searches. Int J Numer Meth Eng 2003;58(7):999–1048.

[8] Barenblatt GI. The formation of equilibrium cracks during brittle fracture. General ideas and hypotheses. Axially-symmetric cracks. J Appl Math Mech-USS 1959;23(3):622–36.

[9] Hillerborg A, Modéer M, Petersson PE. Analysis of crack formation and crack growth in concrete by means of fracture mechanics and finite elements. Cem Concr Res 1976;6(6):773–81.

[10] Chen J, Crisfield MA, Kinloch AJ, Busso EP, Matthews FL, Qiu Y. Predicting progressive delamination of composite material specimens via interface elements. Mech Compos Mater St 1999;6(4):301–17.

[11] Tvergaard V, Hutchinson JW. The influence of plasticity on mixed mode interface toughness. J Mech Phys Solids 1993;41(6):1119–35.

[12] Scheider I, Brocks W. Simulation of cup–cone fracture using the cohesive model. Eng Fract Mech 2003;70(14):1943–61.

[13] Petersson PE. Crack growth and development of fracture zones in plain concrete and similar materials. Report TVBM-1006. Division of Building Materials, Lund Institute of Technology (Sweden) 1981.

[14] Xu XP, Needleman A. Numerical simulations of fast crack growth in brittle solids. J Mech Phys Solids 1994;42(9):1397–434.

[15] Alfano G. On the influence of the shape of the interface law on the application of cohesive-zone models. Compos Sci Technol 2006;66(6):723–30.

[16] Alfano M, Furgiuele F, Leonardi A, Maletta C, Paulino GH. Mode I fracture of adhesive joints using tailored cohesive zone models. Int J Fracture 2009;157(1–2):193–204.

[17] Raju IS. Calculation of strain-energy release rates with higher order and singular finite elements. Eng Fract Mech 1987;28(3):251–74.

[18] Sørensen BF, Jacobsen TK. Determination of cohesive laws by the J integral approach. Eng Fract Mech 2003;70(14):1841–58.

[19] Hellen TK. On the method of virtual crack extensions. Int J Numer Meth Eng 1975;9(1):187–207.

[20] Parks DM. A stiffness derivative finite element technique for determination of crack tip stress intensity factors. Int J Fract 1974;10(4):487–502.

[21] Liljedahl CDM, Crocombe AD, Wahab MA, Ashcroft IA. Damage modelling of adhesively bonded joints. Int J Adhes 2006;141(1–2):147–61.

[22] Blackman BRK, Hadavinia H, Kinloch AJ, Williams JG. The use of a cohesive zone model to study the fracture of fibre composites and adhesively-bonded joints. Int J Fract 2003;119(1):25–46.

[23] Manzoli OL, Shing PB. A general technique to embed non-uniform discontinuities into standard solid finite elements. Comput Struct 2006;84(10–11):742–57.

[24] Camanho PP, Davila CG, de Moura MF. Numerical simulation of mixed-mode progressive delamination in composite materials. J Compos Mater 2003;37(16):1415–38.

[25] Turon A, Camanho PP, Costa J, Dávila CG. A damage model for the simulation of delamination in advanced composites under variable-mode loading. Mech Mater 2006;38(11):1072–89.

[26] Turon A, Camanho PP, Costa J, Renart J. Accurate simulation of delamination growth under mixed-mode loading using cohesive elements: definition of interlaminar strengths and elastic stiffness. Compos Struct 2010;92(8):1857–64.

[27] Lorentz E. A mixed interface finite element for cohesive zone models. Comput Method Appl Math 2008;198(2):302–17.

[28] Biel A, Stigh U. Effects of constitutive parameters on the accuracy of measured fracture energy using the DCB-specimen. Eng Fract Mech 2008;75(10):2968–83.

[29] Škec L, Jelenić G, Lustig N. Mixed-mode delamination in 2D layered beam finite elements. Int J Numer Meth Eng 2015;104(8):767–88.

[30] Škec L, Alfano G, Jelenić G. Enhanced simple beam theory for characterising mode-I fracture resistance via a double cantilever beam test. Compos Part B-Eng 2019;167:250–62.

[31] Williams JG. End corrections for orthotropic DCB specimens. Compos Sci Technol 1989;35(4):367–76.

[32] de Morais AB. Mode I cohesive zone model for delamination in composite beams. Eng Fract Mech 2013;109:236–45.

[33] Sun CT, Pandey RK. Improved method for calculating strain energy release rate based on beam theory. AIAA J 1994;32(1):184–9.

[34] Sankar BV. A finite element for modeling delaminations in composite beams. Comput Struct 1991;38(2):239–46.

[35] Roche CH, Accorsi ML. A new finite element for global modeling of delaminations in laminated beams. Finite Elem Anal Des 1998;31(2):165–77.

[36] Čas B, Saje M, Planinc I. Non-linear finite element analysis of composite planar frames with an interlayer slip. Comput Struct 2004;82(23–28):1901–12.

[37] Kryžanowski A, Schnabl S, Turk G, Planinc I. Exact slip-buckling analysis of two-layer composite columns. Int J Solids Struct 2009;46(14–15):2929–38.

[38] Kroflič A, Saje M, Planinc I. Non-linear analysis of two-layer beams with interlayer slip and uplift. Comput Struct 2011;89(23–24):2414–24.

[39] Schnabl S, Planinc I. Exact buckling loads of two-layer composite Reissner's columns with interlayer slip and uplift. Int J Solids Struct 2013;50(1):30–7.

[40] Carpinteri A, Massabo R. Continuous vs discontinuous bridged-crack model for fiber-reinforced materials in flexure. Int J Solids Struct 1997;34(18):2321–38.

[41] Rots JG. Smeared and discrete representations of localized fracture. Int J Fract 1991;51:45–59.

[42] Reissner E. On one-dimensional finite-strain beam theory: the plane problem. Z Angew Math Phys 1972;23(5):795–804.

[43] Rodman U, Saje M, Planinc I, Zupan D. Exact buckling analysis of composite elastic columns including multiple delamination and transverse shear. Eng Struct 2008;30(6):1500–14.

[44] The Mathworks Inc. MATLAB version 9.7.0.1319299 (R2019b). Natick, Massachusetts 2019..

[45] da Silva LFM, Rodrigues TNSS, Figueiredo MAV, de Moura MFSF, Chousal JAG. Effect of adhesive type and thickness on the lap shear strength. J Adhesion 2006;82(11):1091–115.

[46] da Silva LFM, Critchlow GW, Figueiredo MAV. Parametric study of adhesively bonded single lap joints by the Taguchi method. J Adhes Sci Technol 2008;22(13):1477–94.

[47] Wieghardt K. Über den Balken auf nachgiebiger Unterlage. Z Angew Math Mech 1922;2(3):165–84.

[48] Biot MA. Bending of an infinite beam on an elastic foundation. J Appl Mech 1936:. A–1.

[49] Reissner ME. On the theory of beams resting on a yielding foundation. Proc Natl Acad Sci USA 1937;23(6):328–33.

[50] Allen HG. Analysis and design of structural sandwich panels. New York: Pergamon; 1969.

[51] Timoshenko S. Strength of materials part 1: elementary theory and problems. New York: Van Nostrand; 1955.

[52] Stanić A, Brank B, Korelc J. On path-following methods for structural failure problems. Comput Mech 2016;58(2):281–306.

[53] Girhammar UA, Gopu VKA. Composite beam-columns with interlayer slip–exact analysis. J Struct Eng-ASCE 1993;119(4):1265–82.

[54] Sheinman I, Soffer M. Post-buckling analysis of composite delaminated beams. Int J Solids Struct 1991;27(5):639–46.